Damage evolution in different types of concrete by means of splitting tests

A. Vervuurt and J.G.M. van Mier
Delft University of Technology, Faculty of Civil Engineering

B. Chiaia
Delft University of Technology, Faculty of Civil Engineering and Politecnico di Torino, Department of Structural Engineering

A new splitting test has been used for evaluating damage in different types of concrete. The set up was developed at the Stevin Laboratory of Delft University of Technology and comprises a completely new loading device in which a perfectly horizontal splitting load can be applied to concrete specimens. In addition to classical mechanical measurements, a high resolution optical microscope has been adopted for crack detection at the surface of the thin specimens. Microscale information was obtained on the topological characteristics of the damage patterns. Fractal dimensions were computed. In total, three cement paste mixtures, four mortars and four different types of concrete will be discussed in this paper. The concretes contained either river gravel with different maximum aggregate size (2 and 16 mm), phosphorous-slag aggregates or Lytag lightweight aggregates. To obtain a better understanding of the failure mechanisms at the interface between matrix and composite, tests were performed where a single (cylindrical) aggregate was embedded in a matrix of cement paste or mortar. It will be shown that the concrete mixture with phosphorous-slag aggregates yields the highest peak load and the most brittle post-peak behavior whereas the concrete with large river gravel aggregates shows the most ductile load-displacement response. Furthermore the interfacial strength is affected substantially by the density of the aggregates. This provides a different failure mechanism for the lightweight concrete as indicated by the microscopic observations. The fractal analysis of the different damage patterns confirmed different behaviors, strictly related to peculiar microscopic mechanisms.

1 Introduction

In heterogeneous materials like concrete, sandstone and rock, the weakest link is generally the zone between two dissimilar materials. For normal weight concrete specifically, the interfacial zone between (mortar or cement) matrix and aggregates is considered to be the weakest element in the material structure (e.g. Mindess 1983). However, it seems that not only the strength of the interface plays a dominant role in crack initiation, but more meaningfull, the combination of stress and strength. In fact, the material is most likely to fail at the point with the highest stress relative to its strength. At the interface between matrix and aggregate, two materials meet with considerable

HERON, Vol. 40, No. 4 (1995) ISSN 0046-7316

difference in Young's moduli. This results in stress concentrations. Combined with the relatively low strength, this (highly porous) zone becomes of major importance for crack initiation.
The process from microcracking to macrocracking is characterized by interfacial cracks growing through the matrix and joining into macrocracks. It was shown that the macro-cracks remain discontinuous during a very long time. In the softening stage of the material the crack faces are still connected by so-called crack face bridges (Van Mier 1991a). These bridges provide for stress transfer, and explain the long stable tail of the tensile softening curve.
In the Fictitious Crack Model (Hillerborg 1976) and in the Crack Band Model proposed by Bažant & Oh (1983), a cloud of microcracks ahead of the macroscopic crack tip has been assumed. This explanation was based on a supposed similarity to the Dugdale-Barenblatt model for metals, see for instance Barenblatt (1962). For concrete however, the method seems mainly based on requirements for analytical treatment of the material behavior rather than on a physical mechanism as was shown in experiments of Van Mier (1991a). Especially the fact that the crack is assumed to be completely stress free seems not very logical for concrete considering the above mentioned crack face bridges. Nevertheless, from a practical point of view, these types of models have proven to give satisfactory results for simulating concrete failure. Therefore the method is well accepted in the sense of non-linear elastic finite element analysis of concrete, although real predictive qualities of the model are still lacking. Generally in the case of the smeared crack method (e.g. Rots 1988), the effect of the crack is *smeared out* over the width of a single finite element. Next to the width of the band of microcracks ahead of the traction-free crack tip, the fracture energy (G_F) is assumed to be a material property. In other words the fracture energy should be a constant value, regardless the size of the specimen or the specific boundary conditions under which failure occurs. The question remains however whether this is true, since G_F is calculated as the work of fracture (W_F) per unit of cracked surface. Normally it is assumed that the work of fracture can easily be determined from the area under the stress-crack opening response from a uniaxial tensile test. In such a test the fracture energy G_F is determined by dividing the total work of fracture W_F by the net area A of the specimen ($G_F = W_F / A$). From experiments, however, a strong size effect is observed (Hillerborg 1985, Elices et al. 1992), indicating that additional energy dissipation occurs outside the localization zone. Moreover, it was shown that the boundary conditions of the specimen affect G_F or at least W_F (Vervuurt & Van Mier 1994a).
In this paper we will not further elaborate on size and boundary condition effects on fracture energy and strength, but rather emphasize the microscopic fracture mechanisms in concretes containing different types of aggregates. In Van Mier (1991a,b) it was already shown that the crack face bridges in lightweight concrete (with d_{max} = 12 mm for Lytag and d_{max} = 4 mm for sand) loaded in uniaxial tension, are of comparable size as bridges observed in a mortar with d_{max} = 2 mm. In lightweight concrete cracks tend to growth through the (weaker) aggregates, whereas in normal weight concrete the cracks are more likely to follow the (weak) interface between aggregate and matrix. Main reasons for this difference in the failure mechanism are the changing ratios of strength and stiffness of the various components in the material structure. In the present study several types of concrete as well as mortars and cement paste mixtures have been subjected to a splitting load.
The damage evolution during the fracture process has been monitored with a long distance optical microscope which has been adapted for automatically (re)scanning the crack path. Moreover, interface failure has been investigated separately in the same type of splitting test containing a single

cylindrical aggregate embedded in a selected matrix of cement paste or mortar. Aggregate types with either a dense or porous interfacial zone have been studied.
A fractal analysis of the damage patterns has been carried out for all the mixtures, including the single particle tests. Image processing algorithms have been developed and coupled with standard routines to extract the crack topology from the digitized images. The Box-Counting method has been applied to the filtered images, in which the fractal characteristics have been highlighted. It is shown that the fractal analysis can successfully describe the progressive vanishing of micro-structural disorder effects, which is related to different scales of observation of the fracture process. Peculiar micromechanisms of failure are involved in each material. Moreover fractality comes into play also at the level of the single aggregate, as well as in the case of the intra-particle cracks occurring in the Lytag composite. No clear correlation can be deduced between the fractal dimensions and the fracture energy values for the different concretes.
In the paper first the experimental equipment used, and data aquisition system are outlined. After that, specimen preparation and characteristics of the materials used will be described. Following to this a detailed analysis of the results is given.

2 Experimental equipment and data aquisition

2.1 *Loading equipment*

In this section the specimen geometry and the experimental set up will be described. Moreover attention will be paid to the data aquisition system of the displacement measurements and to the use of a long distance (optical) microscope. Because the microscope monitors only the surface of the specimen, relatively thin specimens were used. Another reason for the small thickness of the specimens is the aim of the experiments for validating a two-dimensional numerical model (Vervuurt & Van Mier 1995). For both aspects uniform crack growth over the specimen thickness is required. The specimens, with planar dimensions of 125 ¥ 170 mm (see Fig. 1) have a thickness of 10, 15 or 20 mm. In this paper only tests on specimens with a constant thickness of 15 mm will be discussed. No attention will be paid to the 10 and 20 mm specimens and to the numerical aspect of the research program which will be published in a separate paper (Chiaia, Vervuurt & Van Mier 1996).
To fix the position of crack initiation, a 30 mm deep notch was sawn at half width of the specimen. The depth of the notch depends on the unrestricted view at the area near the notch, which is required by the microscope. An open frame has been developed (Fig. 2a) in which the specimen is positioned during testing. The base of the notch is chosen just beneath the upper bar of the loading frame. At the top of the specimen two loading platens are glued, between which a perfectly horizontal splitting load can be applied. The specimen is supported at the bottom with a small strip of steel (15 mm width), since the high resolution long distance microscope requires a fixed position of the specimen for studying the concrete surface. Next to the strip and the two supports to which the load is applied, three spring supports are also attached at the back of the specimen, to ensure co-planarity of the specimen surface and the microscope during the entire loading sequence.
A completely new device (Fig. 2) was developed for applying the load at the specimen. In order to avoid vertical stresses in the specimen during loading, a horizontal splitting load was applied rather than the more common wedge splitting load (which was earlier suggested by Linsbauer and

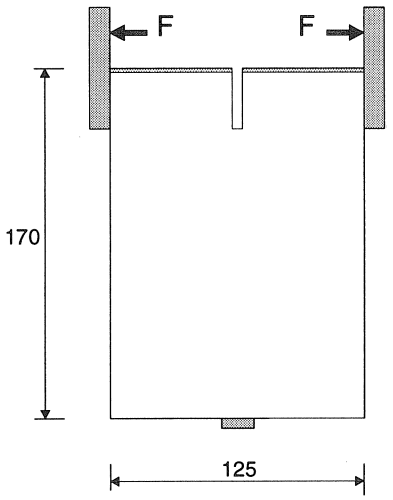

Fig. 1. Specimen geometry. Measurements are given in mm and the thickness of the specimens tested was 10, 15 or 20 mm.

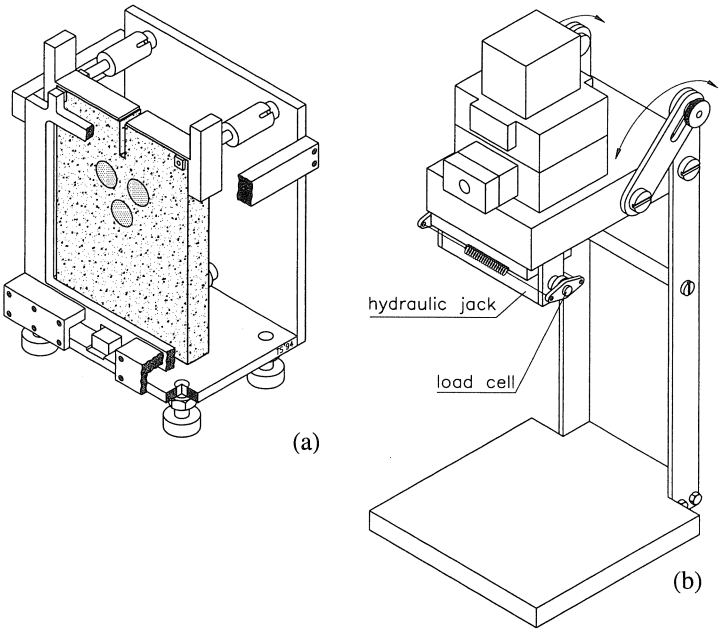

Fig. 2. Experimental set up. During testing the loading frame (a) is centered under the loading device (b).

Tschegg (1986)). In the latter tests, which can be carried out in a standard compression machine, strong frictional effects caused by the wedge may affect the results significantly, especially in the tail of the softening curve. It will be shown in this paper that the cracks are inclined to propagate

along a curved path to the side of the specimen when a pure horizontal splitting load is applied. The load is applied through a symmetric hydraulic actuator, consisting of a single oil reservoir and two pistons, one at each side of the central reservoir. The load is measured using two miniature Sensotec load cells (type LFH-7I/280-01) which can measure a maximum load of 1 kN (250 lbs) each. Both load cells are fastened to the hydraulic jacks in front of the two load-points. The experiments are carried out under displacement control in which the average crack mouth opening displacement (CMOD) is used as feed back signal for the closed-loop servo-controlled system. For the displacement measurements, two LVDTS with a measuring length of 15 mm are glued across the top of the notch, at each side of the specimen. The CMOD is calculated as the average of these two LVDTS and has been monitored either until complete fracture of the specimen occured or until a maximum CMOD approximately equal to 160 μm. In this way it is possible to measure not only the maximum load P_u but the total work of fracture (W_F) as well. From W_F the specific energy dissipation per unit area (G_F) can be calculated. It should be mentioned that these values of G_F have to be interpreted as nominal values, since they are computed by dividing the work of fracture by a nominal fracture area A_{nom} resulting from the (macroscopic) length of the final main crack. For this purpose the crack-length was measured after complete failure of the specimen.

2.2 *Optical microscope*

To retrieve more detailed information regarding the (micro)cracks that develop at the surface of the specimen, real time measurements are performed with a high resolution long distance optical microscope, as mentioned before. A QUESTAR Remote Measurement System (QM100-RMS) has been adopted (Fig. 3). The system was already available at the laboratory for quite some years and has proven to be very useful for explaining failure mechanisms in concrete (Van Mier 1991b). In those early tests the system was suitable for manual scanning only. Recently, however, the system has been adapted for digitizing images and automatically storing and rescanning the crack path. Therefore a new software package for controlling the microscope has been developed and implemented in an existing image processing program (Fig. 3). The image processing program TIM (Ekkers 1991) has been used as a toolbox for post-processing digital images and quite some experience has been obtained with it in geomechanics, where the program has been used for analyzing soil behavior in a geocentrifuge (Stuit 1993). More detailed information on the image processing procedures which have been adopted here will be given in section 5.1.

A schematic view of the complete microscopic system is given in Fig. 3a. The system consists of the QUESTAR microscope (QM100 MK-III) which is connected to an Ikegami (ICD-46E) black and white CCD Camera for retrieving the images. Through a variable scan framegrabber (VP-1400-KIT-768-E-AT) the images are digitized and stored in binary format at the hard disk of a personal computer. The microscope and the camera are fixed on a cradle which can be moved with stepper motors (Compumotor A/AX57-51) in three orthogonal directions. The stepper motors are controlled through a four axis indexer (Compumotor AT6400) from the same PC as where the images are recovered . The accuracy of the stepper motors is approximately 1 μm and the range of each motor is about 50 mm. The microscope operates at a distance of 200–225 mm from the specimen surface, depending on the selected magnification factor. During the test, the specimen is illuminated using two fiber optic arms, connected to a AIMS FB-150 light source.

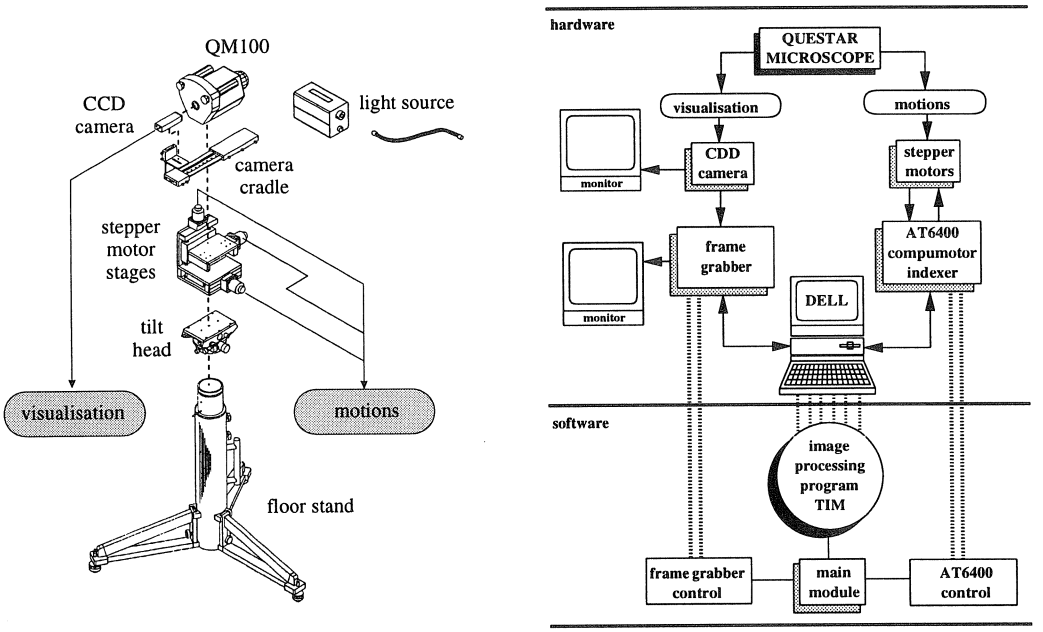

Fig. 3. (a) Schematical view of QUESTAR *QM100 Remote Measurement System* (RMS). *The flow chart in fig. (b) shows the software implemented in the image processing program* TIM *(Vervuurt & Van Mier 1994b).*

The images passed by the camera have a size of 756 × 581 pixels, each pixel representing a gray level between 0 (black) and 255 (white). However for optimal use of the frame grabber, images of 768 × 512 pixels are stored, which results in effective images of 756 × 512 pixels. For scanning the specimen with the microscope, an imaginary grid is projected on top of the specimen, each cell in the grid representing a single image. A small overlap of the images is taken into account in the selected cell size. The microscope provides five different magnification factors, of which only two are used. For practical reasons the largest magnification factor is not used. In this case the roughness of the specimen surface causes focusing problems. In the experiments presented in this paper, the one but largest magnification factor with a resolution of 0.71 pixel/ μm^2 is used for the high resolution images, and the smallest magnification factor (0.28 pixel/ μm^2) is used for retrieving more global information on the microcracks. Another method for retrieving more global crack information is scaling several high resolution images (0.71 pixel/ μm^2) to a 756 × 512 format.
A technique was developed for reducing the images and pasting them together in a mosaic of the completely scanned crack pattern. The reduction factor depends of course on the number of images used in the mosaic. For the numerical procedures adopted for computing the fractal dimensions of the cracks it is also possible to use each disconnected (original) image for retrieving detailed information of the mosaic.

3 Materials characteristics and specimen preparation

Damage evolution was studied in different cement composites subjected to a tensile splitting load. Three different types of hardened cement paste and four mortars were tested along with four concrete mixtures. The mortars and hardened cement paste mixtures, contain only one aggregate (placed at a prescribed location), whereas the concrete mixtures contain a full distribution of aggregates. The experiments regarding the hardened cement paste and mortar will be referred to as *single particle tests*. In this section three subsections are distinguished. In the first subsection, the materials for the single particle tests will be outlined. The composition in the matrix (cement paste and mortar) will be described. Furthermore the materials and positions of the aggregate in the single particle tests are elucidated. In the second subsection, the mix proportions of the four concrete types will be discussed and finally, in the third subsection, the standards tests are described. Again, first the single particle tests (cement paste and mortar mixtures) are discussed, whereafter the results for the concrete mixtures are given.

3.1 Single particle tests

To investigate the specific failure mechanisms in concrete, experiments were carried out in which the interfacial zone between the matrix and composite was studied. For this purpose a special mould was developed in which a single sized, cylindrical aggregate (diameter 20 mm) was positioned a little eccentric beneath the (sawn) notch, as indicated in Fig. 4. This position will be denoted as position P0 and the centre of the aggregate is situated 50 mm left and below the upper right corner of the specimen. To investigate the influence of the aggregate position, four additional locations were studied (P1 to P4 in Fig. 4), positioned 7.5 mm left and right from P0 and 10 mm beneath and above position P0.

For maximum contrast in the microscope images, a white Portland Cement (Blanc BEL P40) was used. Hardened cement paste mixtures with a water-cement ratio of 0.35, 0.40 and 0.45 were tested (Table 1). In the remainder of this paper they will be referred to as CP035, CP040 and CP045 respectively. The mortars, having a maximum aggregate size of the sand of 0.25 mm, were made with three water-cement ratios as well, i.e. 0.40 (MM040), 0.45 (MM045) and 0.50 (MM050).

In addition, a mortar (d_{max} = 0.25 mm) with a superplasticizer having a water-cement factor of 0.40 (MS040), was tested. Superplasticizer was added for improving the manufacturing procedure.

Table 1. Mix proportions for the cement paste mixtures and mortars. Cement and sand fractions as well as superplasticizer quantities are given in kg/m3.

Mixture	CP035	CP040	CP045	MM040	MM045	MM050	MS040
0.125–0.25 mm	–	–	–	813	775	756	813
Cement*	1499	1394	1304	966	922	900	966
w/c ratio	0.35	0.40	0.45	0.40	0.45	0.50	0.40
Superplasticizer**	–	–	–	–	–	–	4.85

* White Portland Cement (Blanc BEL P40).

** TILLMAN OFT4.

A single cylindrical aggregate (Fig. 4) was embedded in each type of cement paste and in each type of mortar matrix according to Table 1. Three different aggregate types were studied. Because the density of the interfacial zone strongly influences the failure mechanism in this region, a dense and a porous type of aggregate type tested. Using Bentheimer sandstone from Germany a denses-interface was created. This case is comparable to concrete containing Lytag aggregate particles. Unfortunately, Lytag was not available in large dimensions as required for the cylinders in the single particle tests. Opposed to the porous aggregate, a dense granite aggregate (Polar White granite from Brasil) was used, having a high particle strength and a weak interfacial zone compared to the sandstone. Furthermore, cylinders were cored from several blocks of phosphorous-slag and embedded in the MS040 matrix. These results were compared to the concrete specimens with the same type of slag and matrix (ConPS, as will be explained in the next subsection). To study the influence of the aggregate position, five different aggregate locations were tested for the specimens where a sandstone particle was embedded in the MS040 matrix, as indicated in Fig. 4b.
The cement paste and mortar specimens were casted in a mould measuring $396 \times 310 \times 120$ mm^3. The cylindrical aggregates were dried in an oven at 105 °C for 24 hours and preserved in silica gel. Just before casting, the aggregates were positioned in the mould. Since it was expected that the moisture content of the sandstone would influence the interface properties it was decided to use wet sandstone aggregates as well. It was found, however, that the results between the wet and dry sandstone aggregates did not differ substantially. Therefore no special attention will be given to this variable in this paper. Demoulding and curing conditions were the same as for the concrete specimens. The specimens were sawn after 14 days of hardening and tested at an age varying between 15 and 18 days.

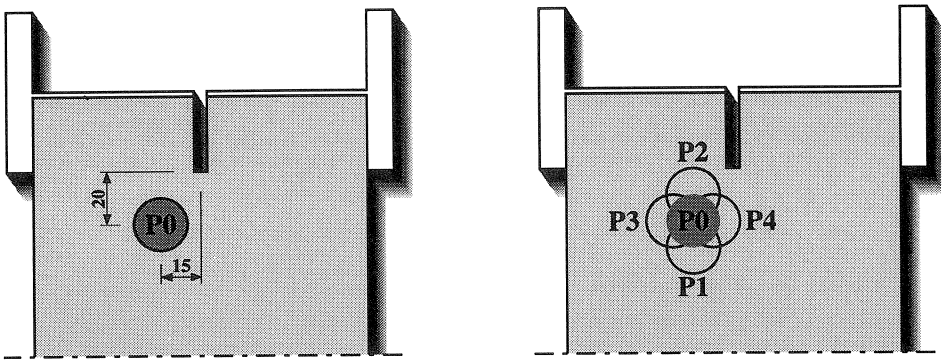

(a) (b)

Fig. 4. Studied aggregate positions (P1 to P4) referred to the origin of position P0.

3.2 *Concrete mixtures*

For the concrete mixtures several types of aggregate were used. Specimens were casted using traditional river gravel having a maximum aggregate size of 16 mm (Con16) or 2 mm (Con2). Because of increasing interest in environmental issues, industrial rest-products are used more frequently now-

adays for the fabrication of aggregate particles for concrete. A mixture was made containing phosphorous-slag (ConPS) instead of river gravel as aggregates. Phosphorous slag is the dross seperated in a fused state during the extraction of phosphor from natural minerals. The slag closely resembles some vulcanic scoria, and the vitreous consistency accounts for its hardness and strength. Improved mechanical performance is obtained if the product is poured out and cooled under controlled conditions. The matrix in the (4–16 mm) slag concrete was taken equal to the MS040 mortar. Next to this very dense type of aggregate also an extremely lightweight aggregate was used. Such aggregates can be very useful when the dead weight of a structure has to be minimized. In the present study Lytag particles were used. Lytag is produced by sintering pulverized fly-ash (released as a rest-product in coal-burning energy power plants) mixed with powder coal particles. More detailed information on the concrete mixtures is given in Table 2.

Table 2. Mix proportions for the tested concrete mixtures. Cement and sand fractions as well as superplasticizer quantities are given in kg/m3.

Concrete Mixture	Con 16	Con2	ConPS	Lytag
8.0–16.0 mm	457	–	–	–
4.0–8.0 mm	365	–	–	–
2.0–4.0 mm	256	–	–	75
1.0–2.0 mm	256	500	–	150
0.5–1.0 mm	220	514	–	150
0.25–0.5 mm	165	197	–	225
0.125–0.25 mm	128	303	506	150
Phos.Slag 4.0–16.0 mm	–	–	1000	–
Lytag 6.0–12.5 mm	–	–	–	464
Lytag 4.0–8.0 mm	–	500	–	249
Cement*	375	250	602	320
w/c ratio	0.5	0.5	0.4	0.5
Superplasticizer**	–	–	3.0	–

* White Portland Cement (Blanc BEL P40).

** TILLMAN OFT4

At least two different batches were prepared for each mixture. The four types of concrete were casted in a mould of $200 \times 200 \times 200$ mm^3. The Lytag aggregate particles were placed in fresh tap water one day before casting, in order to completely saturate the highly porous material. Subsequently the particles were (surface) dried for about 24 hours under lab conditions (note that the dry material can absorb up to 20% of water). One day after casting, the blocks were demoulded and placed under water. After 28 days of hardening, the specimens were sawn from the central part of

the block and placed back under water until one hour before testing. The age at testing varied between 29 and 32 days after casting.

3.3 *Standard tests*

For reference, (load-controlled) standard tests were performed to characterize the mixtures. For the cement paste mixtures and mortars, tests were performed according to the Dutch standards. In this standard test an un-notched prism with dimensions $40 \times 40 \times 160$ mm^3 is subjected to a three point bending load. The support span in the tests is 100 mm. Subsequently, the two halves of the prism after failure are loaded in compression, using 40 mm square loading platens. Because the single particle tests were performed at an age of the specimens varying between 15 and 18 days, it was decided to test 6 prisms: three were tested after 15 days of hardening and the remaining three prisms at an age of 18 days. The test results from the prism tests are given in Table 3. The nominal stresses were computed by dividing the measured load by the net area (40×40 mm^2) of the prism. The standard tests confirmed, as expected, an increasing strength for decreasing water-cement ratio. Compared to the flexural strength, the increase of the compressive strength was more pronounced. The strength of the mortars was generally higher than the strength of the cement paste mixtures. The oldest prisms (18 days) showed a flexural strength which was about 5% higher than the specimens tested at 15 days. For the compression tests the difference was 4%.

Table 3. Strength results for the standard prisms at 15 and 18 days age respectively. The average strength results are followed between brackets).

	Flexural strength f_{cf} in MPa		Compressive strength f_{cc} in MPa	
Mixture	15 days	18 days	15 days	18 days
CP035	11.1 (0.4)	11.6 (0.7)	77.0 (0.8)	81.0 (0.9)
CP040	11.2 (0.4)	12.3 (0.4)	65.5 (0.6)	66.7 (1.5)
CP045	9.8 (0.3)	10.3 (0.2)	49.6 (1.5)	52.1 (0.6)
MM040	12.4 (0.3)	12.4 (0.2)	71.9 (0.5)	73.5 (0.7)
MM045	13.1 (0.4)	12.4 (0.6)	66.3 (1.0)	69.0 (0.6)
MM050	9.9 (0.2)	11.4 (0.3)	53.6 (1.4)	56.2 (1.9)
MS040	13.2 (0.3)	13.3 (0.3)	77.8 (0.5)	79.9 (0.6)

For quality control of the concrete mixtures, standard compression and tensile splitting tests were carried out on 150 mm cubes. Each batch included 6 cubes. The results of these tests are given in Table 4.

Table 4. Strength results for the compression and splitting tests on 150 mm cubes for the different types of concrete.

Concrete mixture	Mean compressive strength, f_{cc} (MPa)	Mean splitting tensile strength $f_{ct,spl}$ (MPa)
Con 16	54.4	3.7
Con2	51.0	3.9
Lytag	40.9	3.1
ConPS	74.7	4.8

4 Test results

4.1 *Failure in different types of concrete*

Deformation-controlled splitting tests on the notched specimens have been carried out, and the load-CMOD diagrams have been monitored up to the complete fracture of the specimens (Fig. 5 and 6). Since the maximum CMOD is widely fluctuating among the specimens, a more consistent evaluation of toughness can be obtained by computing the work of fracture up to CMOD = 100 μm, which was reached in almost all the experiments. From this work of fracture the material's nominal fracture energy G_F, could be calculated.

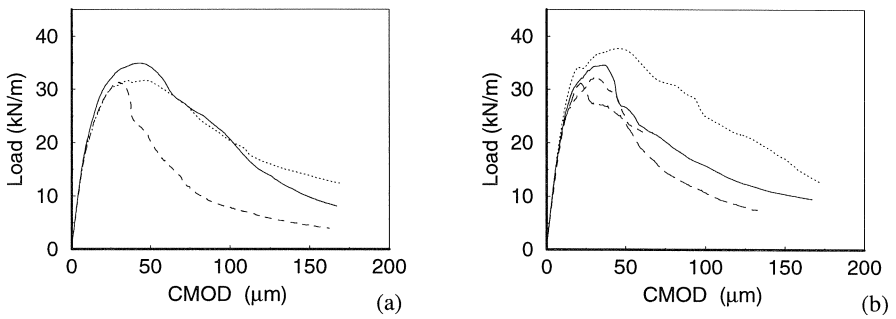

Fig. 5. Experimental load-CMOD curves from splitting tests. Results for Con2 (a), and Con16 (b).

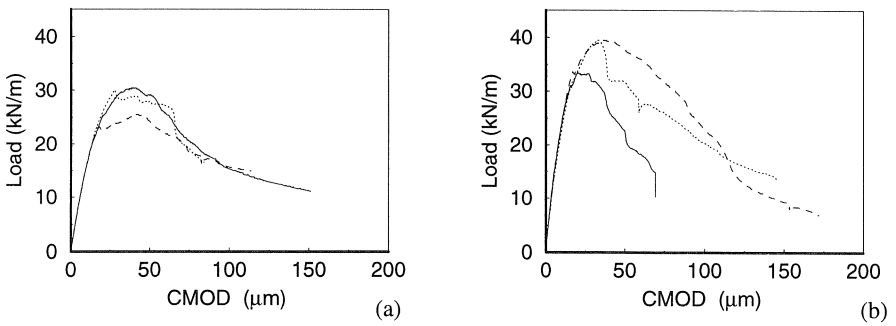

Fig. 6. Experimental load-CMOD curves from splitting tests. Results for Lytag (a), and ConPS (b).

A minimum number of three specimens was tested for each batch of concrete. The strength results of these are reported in Table 4. From this table it can be seen that the phosphorous-slag concrete (ConPS) shows the highest peak load, whereas Con16 is characterized by the highest fracture energy, indicated in column 6 and 7 of Table 5. Note that the G_F values are strongly dependent on the computed crack length. If the 100 μm work of fracture (W_F) is selected as a representative measure of toughness, it must be concluded that ConPS has the largest toughness.

Table 5. Results from the splitting tests on the four different mixtures. The numbers between brackets indicate the standard deviation.

Concrete Type	Max load P_u (kN/m)	Max CMOD δ_{max} (μm)	Work of fracture W_F ($\delta < \delta_{max}$) (Nmm)	Work of fracture W_F ($\delta < 100$ μm) (Nmm)	Fracture energy G_F ($\delta < \delta_{max}$) (N/m)	Fracture energy G_F ($\delta < 100$ μm) (N/m)	G_F/P_u ($\cdot 10^{-3}$)
Con 16	33.2 (0.6)	134.1 (50.0)	43.4 (18.8)	37.4 (8.5)	40.4 (25.1)	36.1 (13.7)	1.21
Con2	32.6 (0.6)	166.7 (4.0)	47.0 (13.0)	35.5 (7.6)	36.6 (10.5)	27.8 (7.0)	1.12
Lytag	28.5 (1.5)	116.2 (33.5)	35.0 (7.5)	31.6 (2.5)	24.9 (5.7)	22.1 (3.0)	0.87
ConPS	37.2 (1.6)	129.1 (53.4)	46.2 (18.9)	44.4 (4.1)	31.4 (17.0)	30.9 (10.0)	0.84

On the other hand, if the ratio between fracture energy and tensile strength is taken as a measure of ductility, phosphorous-slag concrete is the most brittle of the four mixtures, whereas Con16 is the most ductile material. Indeed, this can be expected if one observes the slopes of the softening branches, which are steeper in the case of the ConPS. In fact, this material is characterized by pronounced local instabilities, probably due to the high stiffness of the phosphorous aggregate, which leads to rather brittle interface cracking, as will be clarified in the next section.

The relative brittleness of lightweight concrete is usually explained from the weakness of the Lytag particles, which causes a limited crack-arresting capacity. On the other hand, as it has been detected by the single-particle tests, intra-particle cracks may also propagate in a stable manner , at least this was observed in sandstone particles (see the next section). Lytag particles can be considered strongly heterogeneous at a low level of observation. The fractal dimension of cracks through these particles can be considerable, i.e. when compared to the fractal dimension at the macrolevel of observation. This will be explained in detail furtheron in this paper. This may be the reason for the relevant ductility (G_F/P_u, given in the last column of Table 5) found in the Lytag concrete, which is not trivial when compared to its low nominal fracture energy and strength.

The results of the Lytag and the Con2 are characterized by a much lower scatter in the mechanical properties, as compared to the Con16 and ConPS. In the case of the Lytag, quite remarkably, the three load-CMOD curves almost overlap. This can be explained by the *lower degree of microstructural disorder* at the specimen level. The lightweight concrete is characterized by uniform mechanical properties for both the matrix and the particles. The Con2 is a finer-grained mixture. As it will be

explained furtheron, a more rapidly vanishing fractality occurs in these materials, accompanied by less pronounced scaling effects (Carpinteri and Chiaia 1995).

4.2 *Single particle tests*

To elucidate the most significant effects of the type of aggregate, two examples are given in Fig. 7, 8 and 9. The figures show the observed final crack patterns and the load-CMOD curve for a single aggregate at position P0 (see Fig. 4) embedded in a mortar matrix. Failure in a specimen with a granite aggregate starts at the notch, which is related to the first peak in the load-CMOD curve (Fig. 7a). However, because of the presence of the aggregate, the crack is arrested and a second increase of the load is found. The density of the granite causes the interface to be relatively weak, which results in a second (steep) drop of the load while the crack grows along the interface. At this stage the measured curve joins the diagram of the plain mortar test (i.e. without any large aggregates), as indicated very clearly in Fig. 7a. It should be mentioned, however, that quite some scatter was observed, and the joining of the curves might be coincidental. Cracking proceeds to the left edge of the specimen (Fig. 7b) and is reflected by the final softening branch in the load-CMOD curve. The fact that the crack initiates at the notch instead of along the interface like in normal concrete, can be explained by the fairly large dimensions and isolated location of the single particle. In Fig. 8 four stages of cracking during the fracture process are reported. Each image containes 4 high resolution images (0.71 pixel/μm^2) pasted in a mosaic. From Fig. 8a and 8b it can be seen that cracking just past the first peak is not continuous at all, however the crack has localized already. The image in Fig. 8b is monitored just before the second peak is reached. At this stage some microcracks have already developed in the interfacial zone. In the stages after the second peak (Fig. 8c and 8d) the crack is fully developed and only further crack opening is observed. When a sandstone aggregate is used (Fig. 9) the crack is more likely to grow through the aggregate, instead of along the interface. Moreover, the second peak in the load-CMOD curve is much higher than in the case of the granite. For the specimen containing a sandstone particle it should be mentioned that not all cracks grew through the aggregate. Depending on the porosity of the interfacial zone, also interface cracks could occur. Pores in the interfacial zone were mainly caused by less good compaction during manufacturing of the specimen.

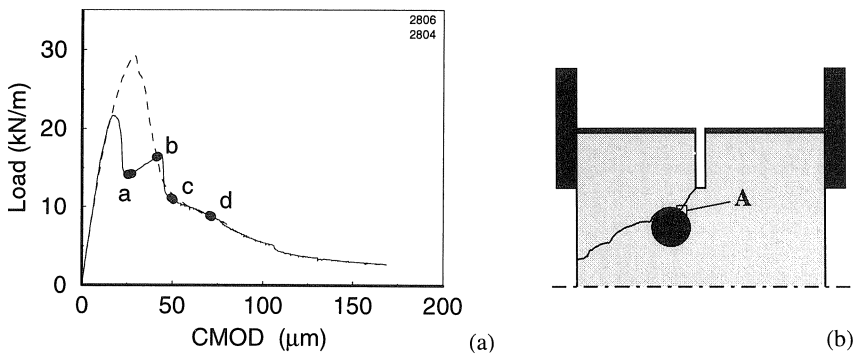

Fig. 7. Results for a granite aggregate in a mortar matrix (MM045): (a) load-CMOD response and (b) final crack pattern. The dotted line shows the response of a similar experiment without large aggregate. The points a to d refer ro the stages of cracking in area A shown in Fig. 8.

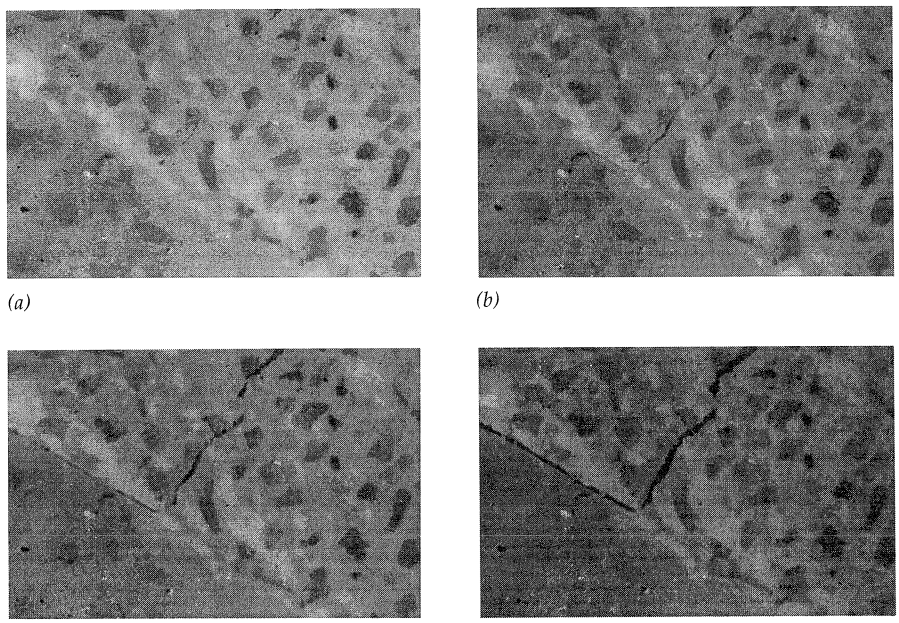

Fig. 8. Cracking history for the specimen of Fig. 7.

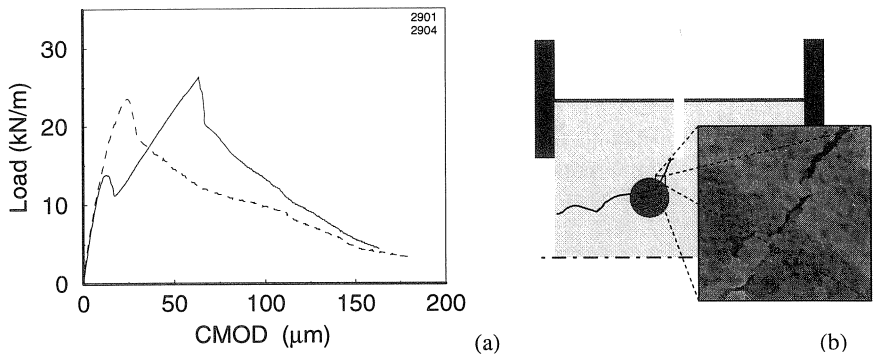

Fig. 9. Load-CMOD response (a) and (b) final crack pattern for a specimen with a sand-stone aggregate embedded in a mortar matrix (MM040). The dotted line shows an experiment without the large aggregate and the inset shows a detail of the interfacial zone.

The results for all four aggregate types embedded in a MM040 matrix (at position P0) are summarized in Table 6. The maximum load (P_u) and the corresponding CMOD (δ_u) characterize the first peak. The (uncracked) specimen stiffness can be extracted from the slope of the pre-peak load-CMOD curve (E_{s1}), and is calculated with the least square method using 15 following measuring points. Because cracking always initiates at the notch, it would be expected that the load at the first peak

did not differ too much for the various aggregate types. However, because of the difference in stiffness between sandstone and granite, the latter shows a higher (first) peak. Since stress concentrations are avoided when no aggregates are embedded, the highest peak-load is measured in these kind of specimens. Only minor differences are observed when the wet and dry sandstone are compared.

The effect of the aggregate location is given in Table 7. The positive slope before the second peak is reached is indicated as E_{s2}. It is mentioned that only one test succeeded until now for location P4. The effect on the peak-load and stiffness seems contradictory when position P0, P1 and P3 are compared to P2 and P4. However, because P2 and P4 are relatively close to the notch a crack initiates at a rather early stage compared to the other aggregate locations. The initial specimen stiffness is a little lower for P2 and P4 while the second slope (E_{s2}) is much higher, which seems a logical consequence considering the aggregate position.

Table 6. Leak loads, CMOD at the peak, and (initial) specimen stiffness for various aggregate types embedded in a MM040 matrix at position P0 (standard deviation between brackets).

Aggregate type	P_u (kN/m)	δ_u (μm)	E_{s1} (GPa)
Sandstone Wet	13.7 (0.4)	13.8 (0.5)	1.7 (0.07)
Sandstone Dry	14.8 (0.8)	17.7 (1.0)	1.5 (0.03)
Granite	17.7 (0.5)	18.4 (1.2)	1.7 (0.05)
No Aggregates	22.3 (0.5)	29.7 (3.9)	1.6 (0.01)

Table 7. Influence of the aggregate position on the peak load and stiffness for sandstone in a MS040 matrix (standard deviation between brackets).

Aggregate position	P_u (kN/m)	E_{s1} (GPa)	E_{s2} (GPa)
P0	23.6 (2.7)	1.91 (0.05)	0.34 (0.07)
P1	23.1 (1.4)	1.97 (0.03)	0.23 (0.03)
P2	15.9 (0.4)	1.74 (0.02)	0.58 (0.02)
P3	25.5 (0.7)	1.92 (0.05)	0.16 (0.00)
P4	17.9 (0.0)	1.74 (0.00)	0.52 (0.00)

5 Image processing and fractal analysis of digitized crack patterns

5.1 *Image filtering and crack extracting*

In addition to the classical load and deformation measurements, optical detection of the (progressively) propagating cracks has been performed in a small region around the notch tip (in order to obtain microscopic damage information). The automatic scanning of the specimen surface during the loading process has been carried out by means of the computer-controlled QUESTAR QM100-RMS described before. After storing the images in the computer, the system automatically scans the prescribed path on the specimen surface. The path along which images are taken is adjusted as cracking proceeds.

After breaking of the specimen, mosaics are created by the computer by linking the single images belonging to a prescribed crack path. The obtained mosaic is stored as a 756×512 pixel image, thus resulting in a lower resolution with respect to the original image. It will be shown that the mosaics represent a more global view of the damage. Therefore, they can be used to properly describe the transition from the fractal disordered patterns detected at the highest magnifications to the Euclidean domains which are usually observed when the scale of observation decreases.

In order to extract the topological information about the damage patterns, filtering of the images is necessary. Starting from complex gray level images (Fig. 10), pixels belonging to the cracks have to be selected and isolated. Due to the dark colour of the cracks, *thresholding* has proven to be the most effective routine. However, this does not turn into a straightforward procedure since discrimination between cracks and dark particles is extremely difficult, as it can be realized by considering the relatively homogeneous histogram of gray values (Fig. 10a). Moreover, especially at the highest magnification factor, three-dimensional assets provide digitization of through-the-depth pixels and affect the proper detection of the crack lips (Fig. 10b). Therefore, prior to thresholding, enhancing the contrast in the image is a useful tool to distinguish more clearly the crack boundaries from their surrounding. This was obtained by eliminating a sufficient number of gray levels to yield a discontinuous histogram (Fig. 11a and 11b). Next, the filtered images have been thresholded and arrays of black and white pixels were generated (Fig. 12a and 12b). Because a unique gray level threshold could not be adopted for a single image, selective filtering has been applied to different parts of the image, choosing for each zone the most appropriate threshold value. This gray level usually ranged between 80 and 135. Minor corrections were sometimes necessary to eliminate isolated black pixels.

After thresholding, binary thinning of the cracks was applied in two different ways. The first algorithm was a commercial one which yielded skeletonized cracks by averaging black pixels through the width (Fig. 13a). A serious drawback was the loss of many details from the crack boundaries, resulting in smoother thinned patterns, not properly representing the complexity of the energy dissipation which takes place at the crack lips. It was therefore decided to develop a second algorithm which was capable to skeletonize the cracks by isolating their boundaries. This approach proved very successful in the case of single cracks propagating along one main direction, since boundaries can easily be detected by scanning the image perpendicularly to the advancement direction (Fig. 13b). On the other hand, when self-similar patterns were digitized, the first algorithm prevailed.

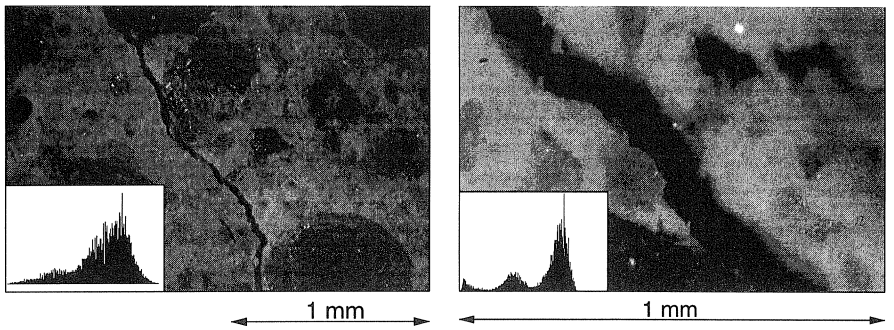

Fig. 10. Digitized binary images before filtering and histogram of the gray values. Standard resolution image of Lytag (a) and high resolution image of Con2 (b).

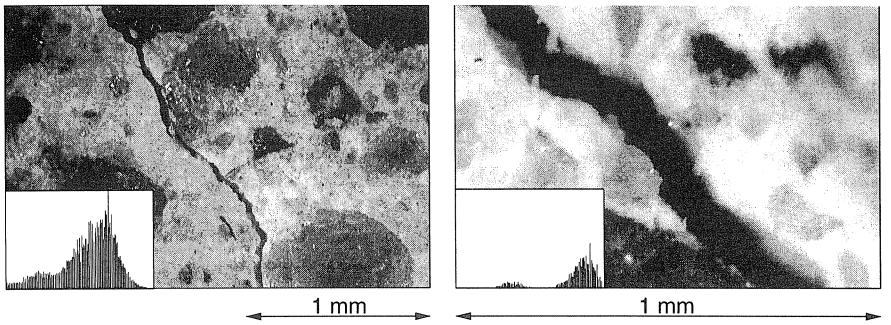

Fig. 11. Digitized binary images after enhancing contrast (discontinuous histogram). Standard resolution image of Lytag (a) and high resolution image of Con2 (b).

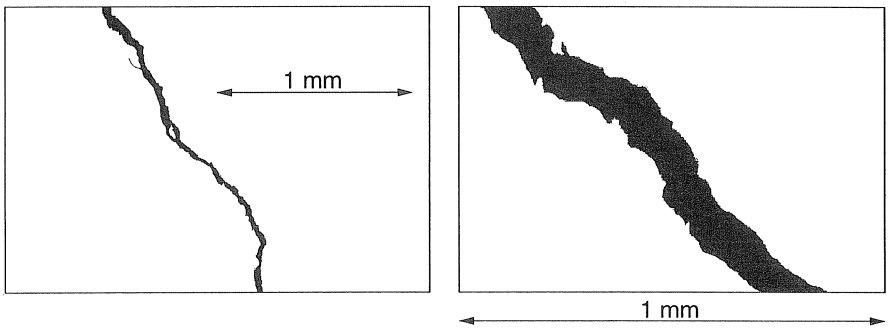

Fig. 12. Digitized crack patterns after multiple tresholding. Standard resolution image of Lytag (a) and high resolution image of Con2 (b).

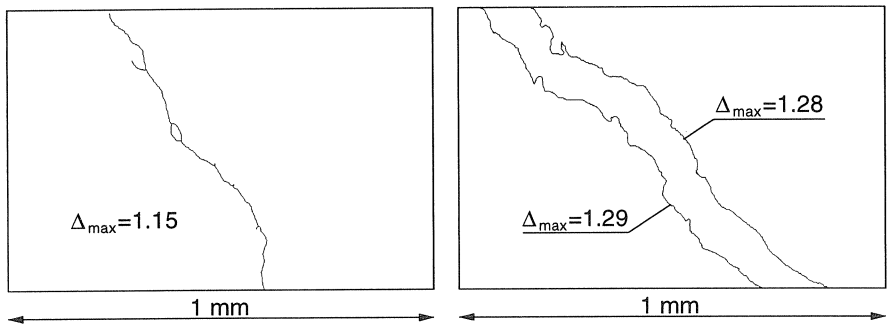

Fig. 13. Two different approaches to the binary thinning of the threshold images. Meanvalue skeletonizing of a standard resolution image of Lytag (a) and boundary outlining of a high resolution image of Con2 (b).

5.2 *The Box-Counting method*

Three definitions of fractal dimension are usually encountered in the literature: the self-similarity dimension, (also called "heuristic"), the Hausdorff dimension and the Minkowski-Bouligand ("covering") dimension (Mandelbrot 1982). The Hausdorff definition is the oldest and probably the most important. It is defined for any topological set (fractal and Euclidean sets). It is also mathematically convenient, because it is based on the concept of the "measure of a set". On the other hand, it is hard to implement in a numerical algorithm.

The self-similarity definition comes directly from the morphological invariance of fractal sets under scale-transformations. The intuitiveness of the self-similarity definition has often mislead researchers, since not all the fractal sets are self-similar. Fractals in nature are usually characterized by self-affine or *multifractal* scaling. In the case of disordered materials, this is due to the presence of a microstructural characteristic length, which plays the role of a crossover between two scaling regimes (Carpinteri and Chiaia 1995). An infinite spectrum of exponents is necessary to describe the entire scaling range of multifractal sets (for example the fracture surfaces), whereas mathematical fractals, lacking any internal length, can be characterized by a unique value of the self-similarity dimension. Therefore, the Minkowski-Bouligand dimension represents the more suitable definition for implementing in numerical codes. The so-called *Minkowski-cover* of a set is obtained by covering the considered domain by means of a collection of regular Euclidean figures, with dimension equal to the space in which the fractal is embedded. The fractal dimension is obtained by computing the *logarithmic density* of the measure of these coverings, as their linear size decreases.

The Box-Counting method, originally proposed by Mandelbrot (1982), represents the most general deterministic method for the case of natural fractals. It can be applied, by means of a unique formulation, either to invasive (fracture surfaces) or to lacunar (isolated cracks) fractals , whereas other classical methods (e.g., the Divider and the Variation method) can only be applied to single fracture profiles (Carpinteri and Chiaia 1995). In order to study the complex crack patterns resulting from the splitting tests, a full-purpose version of the method has been developed. The algorithm, specifically designed for two-dimensional images, can basically be described by the following steps:

- generation of a regular rectangular grid, with linear dimension ε_i and shape factor ρ ($\rho = 1$ corresponds to square boxes);
- covering of the fractal domain by means of the grid (Fig. 14c) and computing the total number of boxes N_i necessary to cover the entire damage pattern (or, equivalently, computing their area E_i). The values corresponding to different origins of the grid are averaged, thereby eliminating biasing trends in large grids;
- repeating the procedure by means of similar grids with progressively decreasing linear size ε_i (Fig. 14d), until the resolution becomes comparable to the discretization interval of the image examined (which is equal to the pixel's linear size in the case of the thinned images) and
- finally, from the mathematical definitions, the *box-dimension* Δ, which can be considered equal to the fractal covering dimension (Minkowski-Bouligand dimension), is obtained as

$$\Delta = \lim_{\varepsilon_i \to 0} \left(\frac{\log N(\varepsilon_i)}{\log(1/\varepsilon_i)} \right) = 2 - \lim_{\varepsilon_i \to 0} \left(\frac{\log[E(\varepsilon_i)]}{\log(\varepsilon_i)} \right) \tag{1}$$

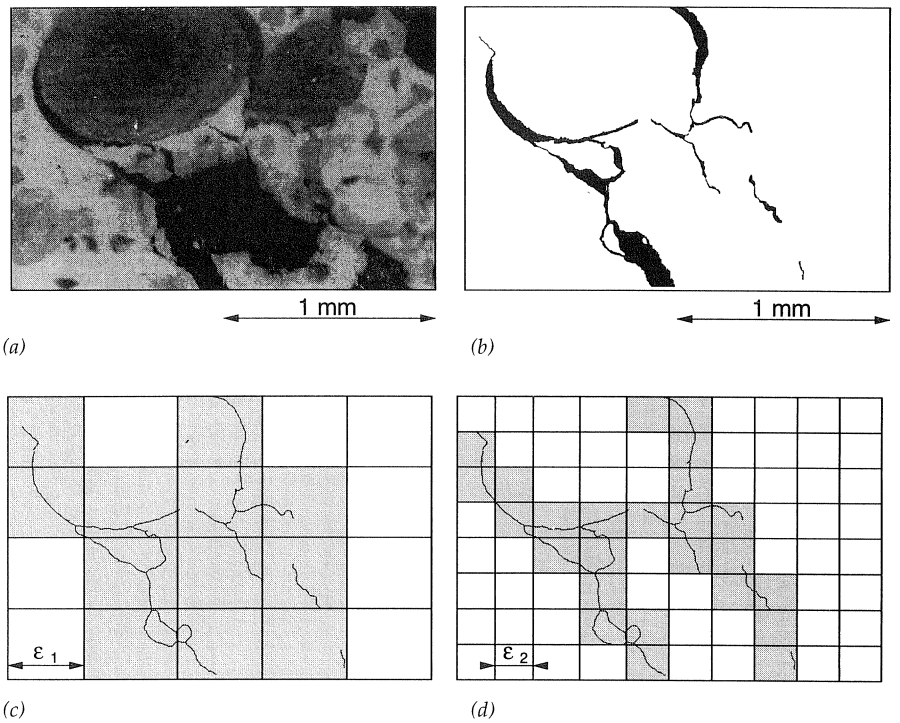

Fig. 14. Mosaic from four high-resolution images on Con2 (a), threshold crack pattern (b), and two steps of the Box-Counting method applied on the skeletonized cracks (c, d). The fractal dimensions Δ in this example is equal to 1.127.

In practical applications, instead of dealing with a limit, the logarithmic density of the coverings is analysed by means of a *linear regression* in the log$N$-logε plot or in the log$E$-logε plot. From these plots the respective slopes ϕ and θ are computed. From these values, the box-dimension is obtained as $\Delta = -\phi$ (Fig. 15) or as $\Delta = 2-\theta$. Note that a typical drawback of the Box-Counting method is depicted by the stepwise data in the log-log plot, due to the fact that N has to be an integer number and, especially when ε is large, some of the boxes are occupied only in a minimum part by the points of the fractal domain, thereby misleading the regression procedure. This trend can be partially eliminated by averaging among different origins of the grid.

Rigorously speaking, the omothetical and progressive shrinking of the covering grids implies isotropic scaling of the covering shape. Self similarity implies that statistically similar morphologies are obtained by isotropic rescaling of the set. This could be in contrast with the eventually anisotropic (self-affine or multifractal) properties of the fractal domain. Therefore, direction-dependent rescaling of the grid size should be performed. If b is the scaling ratio in the x-direction, b^H should be the ratio in the y-direction, where H is the *Hurst exponent* of self-affinity (Mandelbrot 1982). Furthermore, an iterative procedure should be adopted, since the exponent H is not known *a priori*. This relatively awkward procedure can be avoided if anisotropic grids are used. This can be realized by means of rectangular boxes ($\rho \neq 1$), to enhance the statistical fluctuations in one direction. This approach revealed particularly effective in the case of the *post-mortem* analysis of fracture surfaces obtained from uniaxial tensile tests (Carpinteri and Chiaia 1995), where a strong orthotropy was provided between the (mainly horizontal) crack advancement and the orthogonal direction. Note however that the determination of the width over length ratio of the rectangles is not straightforward.

In case of the splitting cracks, because the advancement direction is significantly inclined and curved, the orthotropy directions continuously change. Moreover, the adopted image acquisition process allows for the detection of crack branching and secondary cracks, whereas the *post-mortem* digitization of the fracture surfaces yields a series of fracture profiles which can be interpreted as one-variable function graphs. Therefore, especially with the highest magnification factor, it seems more convenient to use isotropic square coverings of the image cracks, since damage at that scale looks self-similar rather than self-affine.

Indeed, direction-dependent scaling arises as the magnification factor decreases. That is, looking at the cracks from a larger distance, self-affine aspects increase. In this case, rectification of the curvilinear thinned cracks can be exploited, in order to subsequently enhance the fluctuations or thogonal to the advancement direction.

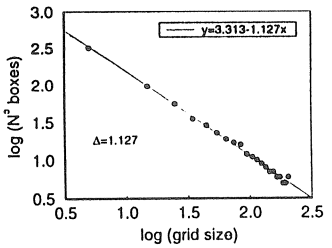

Fig. 15. Application of the Box-Counting method to the skeletonized Con2 image in Fig. 14. Linear regression in the log-log plot and fractal dimension (monofractal hypothesis).

5.3 *Fractal characteristics of the digitized crack patterns*

The optical detection of the damage ahead of the crack tip permits to highlight some morphological differences in the fracture behavior of the different concretes, which correspond to the previously described mechanical differences. The interface between large aggregates and matrix represents the weakest link of the four composites. In the case of the ConPS, the propagation of the cracks is almost totally controlled by the bond strength, and the irregular shape of the aggregates contributes to raise the toughness characteristics. On the other hand, when the aggregate strength is comparable to the strength of the matrix, interface properties play a less pronounced role. A lead role is also played by the porosity of the particles, which enhances the bonding strength as in the case of Lytag (Zhang & Gjørv 1990).

In the case of Lytag and Con2, peculiar aspects of a more homogeneous behavior (at the specimen level) are pointed out, like cracks occurring through the particles in the Lytag and the relative smoothness of the fracture patterns in the Con2. On the other hand, microscopic bridging is activated at the scale of sand grains in the Con2, as well as rough fractal cracks grow through the Lytag particles. This means that disorder is equally present in those two materials, but at *a lower level* of observation as compared to Con16 and ConPS.

The fractal analysis of the filtered cracks has been performed on the thresholded as well as on the skeletonized images. Non-integer topological dimensions of the damage patterns have been found, by means of the Box-Counting method, in all four mixtures. This confirms that, at the proper scales, the phenomenon of fracture in heterogeneous media possesses a well-defined fractal character.

Application of the Box-Counting method on the thresholded images has to take into account the crack opening. If a minimum box size equal to one pixel is used, fractal dimensions close to 2 are computed in the limit of the smallest scales, because the crack is treated as a two-dimensional area. Therefore, a minimum grid size equal to the average crack width was adopted, ranging between 10 and 35 pixels. Unfortunately, many details of the boundaries are missed in this way, and biasing can still occur if a variable crack width is encountered through the image. Nevertheless, especially in the case of self-similar damage, fractal dimensions obtained from simply thresholded images are considered to be consistent.

A minimum box size equal to one pixel (which means roughly 1.4 μm^2 and 3.7 μm^2, respectively for the highest and the lowest magnification factor) has been adopted for analysing the thinned crack patterns. When self-similar damage was detected, through-the-width skeletonizing was often compared with boundary skeletonizing, yielding approximately the same results. Boundary thinning was always preferred in presence of self-affine patterns, since in this way it was possible to enhance the crack lip's irregular fluctuations orthogonally to the advancement direction. Thereby, the local fractal dimension was calculated.

The Box-Counting analysis was carried out on the high resolution images as well as on the standard resolution ones. Moreover, the method was also applied to some of the mosaics, whose resolution depended on the number of pasted images. A general trend has been revealed for the four different concretes: as the resolution of the image decreases, the fractal dimension decreases as well.

An example is shown in Fig. 16a, where the mosaic (whose resolution is approximately equal to 0.07 pixel/μm^2) yielded $\Delta = 1.19$, whereas the standard image (Fig. 16b), corresponding to the lower right corner of the mosaic, yielded $\Delta = 1.26$. It is mentioned that not a unique slope (*monofractality*) can be obtained from the Box-Counting analysis of an image, but a progressively decreasing

slope is obtained as the linear size of the grid increases (Fig. 17). The aforementioned non-linearities witness the transition from fractal microscopic topologies towards homogeneous patterns at larger scales (*geometrical multifractality*) that occurs in the damage evolution of the four concretes. Multifractality implies the progressive homogeneization of the microstructural fluctuations, which is reflected by progressive vanishing of the scaling properties of disordered materials for increasing structural size (Carpinteri 1994).

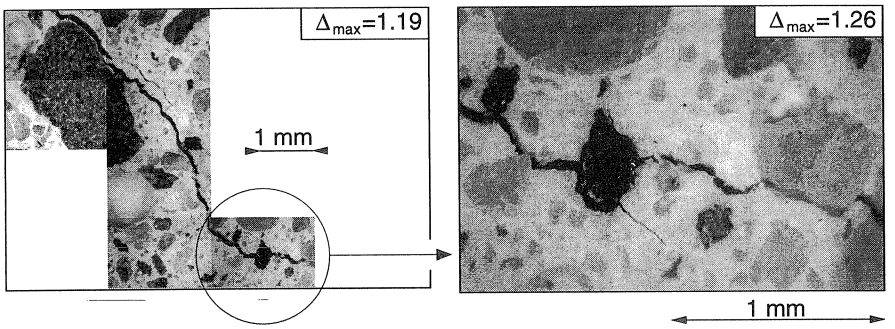

Fig. 16. Damage in the Con16 at various scales of observation. Low-resolution mosaic obtained by pasting seven standard images (a), and standard resolution digitization of one of the images (b).

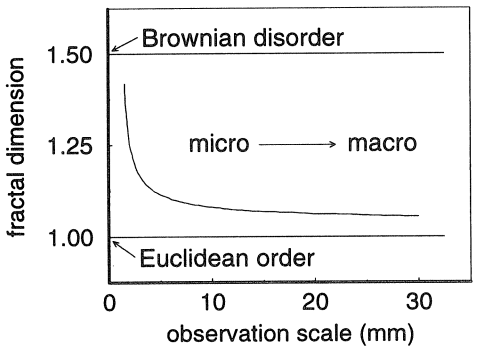

Fig. 17. Geometrical multifractality of the damage patterns in cement-based composites. Transition from microscopic Brownian complexity to macroscopic euclidian order.

In any case, if the mean values of the fractal dimension D of the different concretes are compared (Table 8), it can be stated that homogeneization of the disordered microstructure is observed earlier for the case of lightweight concrete and mortar. Therefore these mixtures can be characterized by a smaller characteristic material dimension. This may explain, as stated before, the lower scatter which has been found in the measurement of their mechanical properties.

Table 8. Measured fractal dimensions.

Image →	High res. (0.71 pixel/μm^2)		Standard res. (0.28 pixel/μm^2)		High res. mosaic		Standard res. mosaic	
Concrete Type	min ↔ max	mean	min ↔ max	mean	min ↔ max	mean	min ↔ max	mean
Con 16	1.16 ↔ 1.33	1.25	1.09 ↔ 1.22	1.14	1.05 ↔ 1.20	1.13	1.06 ↔ 1.13	1.08
Con2	1.08 ↔ 1.30	1.18	1.07 ↔ 1.19	1.10	1.05 ↔ 1.16	1.10	1.02 ↔ 1.04	1.03
Lytag	1.13 ↔ 1.35	1.24	1.05 ↔ 1.20	1.10	1.04 ↔ 1.15	1.09	1.03 ↔ 1.08	1.04
ConPS	1.14 ↔ 1.29	1.18	1.08 ↔ 1.20	1.14	1.07 ↔ 1.18	1.13	1.05 ↔ 1.14	1.07

5.4 *Stable crack growth as a consequence of fractality*

It was already pointed out by Davidson (1989) that higher fractal dimensions not necessarily imply a higher fracture energy of a material, since disordered fracture patterns may be a consequence of both weak (pores, bonds) and strong (aggregates, inclusions) heterogeneities. In the splitting tests, no clear correlation was found between the computed fractal dimensions and the measured fracture energy. This is most likely because of the multifractality of the considered domains. Instead, the invasive fractal damage provides the typical crack-resistance behavior of each of the heterogeneous materials.

The well-known Griffith criterion for brittle fracture has been extended to the case of fractal fractures by considering a fractal crack with dimension $\Delta_G = 1 + d_G$ instead of the classical smooth crack (Carpinteri and Chiaia 1996). Since the *nature* of the energy dissipation is intimately controlled by the disordered fractal microstructure, the *fractal fracture energy* G_F^* has to be considered. This quantity holds non-integer dimensions $[J][L]^{-(2+d_G)}$. It means that energy dissipation, in the case of heterogeneous materials, can be considered intermediate between surface energy dissipation (LEFM) and volume energy dissipation (Plasticity, Damage Mechanics). Let $a^* = a^{(1+d_G)}$ be the Hausdorff measure of the fractal set where dissipation occurs, and let a be its Euclidean projection. Recalling the Griffith procedure, the rate of change of the energy dW_s which is directly dissipated during crack propagation can be obtained by taking the derivative of a^* with respect to a:

$$\frac{dW_s}{da} = 2 \cdot G_F^* \cdot \frac{d(a^*)}{da} = 2 \cdot (1 + d_G) \cdot G_F^* \cdot a^{d_G} \tag{2}$$

The invasive dimensionality of the damage patterns provides an attenuation of the fracture localization, involving also an attenuation of the stress singularity and, macroscopically, a more ductile behavior of disordered materials. When $d_G = 0$, the classical relations of Griffith and Irwin are obtained.

The fundamental consequence of fractality, physically related to the smoothing of the stress-singularity, comes from equation (2). In the case of smooth cracks, however, the energy dissipation is independent of a (constant toughness during crack propagation). In the presence of fractal cracks the energy dissipation increases with a, following a power-law with fractional exponent equal to the fractal dimensional increment d_G of the fracture domain. If the nominal fracture energy is related to the fractal one, it is easy to obtain:

$$G_F \simeq G_F^* \cdot a^{d_G} \tag{3}$$

which clearly indicates that the presence of disorder introduces non-linearities in the fracture behavior of a linear elastic material. What usually is considered as a material constant during crack propagation, turns out to be an increasing function of the crack length (Fig. 18), thereby implying that *the crack resistance grows during the propagation of the fractal cracks* (R-curve behavior) .

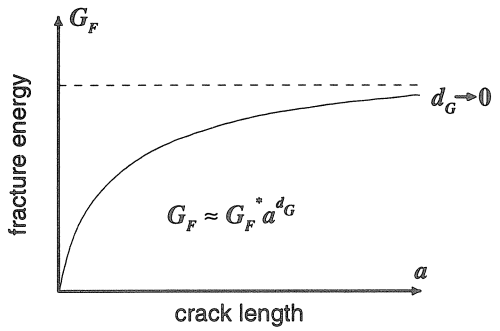

Fig. 18. Stable crack-resistance behavior due to the multifractality of the fracture patterns.

As it was detected experimentally (multifractality), the relevance of disorder decreases as the scale of damage grows (that is, as the crack extension a becomes larger and larger with respect to the microstructural characteristic length l_{ch}). Therefore, since the *global* fractal increment d_G progressively tends to zero as the damage spreads, *a plateau* in the crack-resistance behavior is always detected. This permits to explain the initial *stable crack growth* that has been encountered in the splitting tests.

6 Conclusions

A new splitting test is developed for studying the damage evolution in different types of hardened cement paste, mortar and concrete. A perfectly horizontal load is applied to the specimen, in order to obtain a pure splitting load rather than a combination of splitting and compression. The cracks which develop in the specimen during loading, are automatically monitored with a long distance microscope. In the paper the test technique is described in detail. At present it is possible to continuously monitor crack growth processes in concrete. For further details the reader is referred to Vervuurt (1996). Dedicated image analyses techniques have been developed to analyze the crack patterns. The interfacial transition zone between matrix and composite is studied explicitely in a special specimen geometry containing a single aggregate. The results are used to explain the globally observed material behaviour.

It was shown that the stiffness, strength and density of the aggregates strongly affect the global behavior of the concrete mixture. The vitreous consistency of the phosphorous-slag particles accounts for the high strength, hardeness and relevant fracture energy of the ConPS composite. On the other hand, pronounced local instabilities occur during the loading process, due to the low toughness/strength ratio. This corresponds to sudden debonding of the interface between matrix and aggregate, as was observed in the single particle tests with a stiff granite aggregate as well.

A more brittle structural behavior is therefore provided by this type of concrete, when compared to the normal or Lytag mixtures.
The weakness of the Lytag particles leads to a reduced crack-arresting capacity in the light-weight concrete. A stronger bond between the matrix and the particle results in a more homogeneous damage propagation. Cracks often develop through the particles, and local instabilities (snap-backs) are almost absent. Intra-particle cracks behave in a stable manner due to the microscopic heterogeneity (fractality) of the Lytag aggregates (Table 8), resembling the microscopic complexity revealed in the single particle tests on sandstone. This may be the reason for the relevant structural ductility found for this composite, which is not obvious if related to its low toughness and strength. Moreover, a reduced sensitivity to thermic and drying-shrinkage cracking is present, due to the similar elastic modulus possessed by the matrix and the Lytag aggregates. The behavior of the Lytag mixture seems comparable to the single particle tests when a sandstone aggregate is embedded in a matrix. The high porosity of the aggregate, causes a dense and strong interface.
The globally observed failure mechanism is affected substantial by the strength ratios of the three phases in the material, i.e. matrix, aggregate and bond between matrix and aggregate.
The position of the aggregate in the single particle tests seems of less importance. However, for specimens with an aggregate relatively close to the notch, cracking initiates at a rather early stage. After crack initiation, a more stiff specimen behavior and relatively high strength is observed for specimens with the large aggregate closer to the notch.
The variable role of the microstructural disorder on the mechanical properties of materials can be captured adequately by the fractal analysis. In particular, the fractal characteristics of the damage patterns in different cement-based composites are revealed by means of the Box-Counting method. Self-similar as well as self-affine topologies come into play, and the fractal dimension increases as the scale of observation decreases.
The transition from fractal to Euclidean behavior with increasing scale of observation may be regarded as geometrical multifractality. Therefore, no clear correlation can be stated between fractal dimension and fracture energy. However, the crack-resistance behavior of these composites seems to be the main consequence of the microscopic fractality.
Lytag and Con2 show a much lower scatter of the measured mechanical properties, as compared to Con16 and ConPS. This can be explained by a lower degree of disorder which is due to the relative homogeneity between matrix and particles in the case of Lytag, and to the finer microstructure of Con2. Therefore, a more rapid vanishing fractality is observed, revealed by the image analysis. It can also be argued that less sensitivity to size-effects is present in these two composites.

Acknowledgements

The authors are indebted to Mr. A.S. Elgersma for his expert assistance in building the experimental set up and carrying out the experiments. Pelt & Hooijkaas Vlissingen B.V. is acknowledged for providing the phosphorous-slag aggregates. The fellowship for B. Chiaia was provided by the Delft University Fellowship Program and is greatfully acknowledged.

Notations

W_F	work of fracture
G_F	nominal fracture energy
A	net area of the fracture surface
A_{nom}	nominal area of the fracture surface
P_u	splitting load at the peak
δ, CMOD	Crack Mouth Opening Displacement
δ_u	CMOD corresponding to the peak splitting load
δ_{max}	maximum CMOD measured
d_{max}	maximum aggregate size
f_{cc}	standard compressive strength of concrete
f_{ct}	tensile strength of concrete
$f_{ct,spl}$	standard tensile splitting strength of concrete
f_{cf}	standard flexural strength of concrete
E_{s1}	uncracked specimen stiffness
E_{s2}	slope of the load-CMOD curve before the second peak
Δ	Box-Counting fractal dimension
Δ_G	Box-Counting dimension of a fractal crack
d_G	fractional dimensional increment of a fractal crack
N	number of boxes needed to cover a set on the plane
E	area of the boxes covering a set on the plane
ε	linear size of the boxes
b	scaling ratio in the Box-Counting method
H	Hurst exponent of self-affine sets
ρ	geometrical ratio for rectangular boxes
ϕ, θ	slopes in the double-log diagrams of the Box-Counting method
dW_s	rate of dissipated energy during crack propagation
a	Euclidean measure of a smooth crack
a^*	Hausdorff measure of a fractal crack
G_F^*	fractal fracture energy

References

BARENBLATT, G.I. (1962). "The mathematical theory of equilibrium cracks in brittle fracture", *Adv. in App. Mech.*, **7**, 55–129.

BAŽANT, Z.P. and OH, B.H. (1983). "Crack band theory for fracture of concrete", *Mat. & Struc. (RILEM)*, **16 (93)**, 155–177.

CARPINTERI, A. (1994). "Scaling laws and renormalization groups for strength and toughness of disordered materials", *Int'l J. of Solids and Struct.*, **31 (3)**, 291–302.

CARPINTERI, A. and CHIAIA, B. (1995). "Multifractal nature of concrete fracture surfaces and size effects on nominal fracture energy", *Mat. & Struc. (RILEM)*, **28 (182)**, 435–443.

CARPINTERI, A. and CHIAIA, B. (1996). "Crack-resistance behaviour as a consequence of self-similar fracture to pologies", *Int''l J. of Fracture*, to be published.

CHIAIA, B., VERVUURT, A. and VAN MIER, J.G.M. (1996). "Analysis of interface fracture in particle composites", *Eng. Frac. Mech.*, special issue on statistical fracture mechanics (in preparation).

DAVIDSON, D.L. (1989). "Fracture surface roughness as a gauge of fracture toughness: aluminium-particulate SiC composites", *J. Mat. Sc.*, **24**, 681–687.

EKKERS, R.J. (1991). *TIM user manual version 3.3*, Difa measuring systems BV, Breda, The Netherlands.

GUINEA, G.V., ELICES, M., and PLANAS, J. (1992). "Measurement of the fracture energy using three point bend tests: Part 1 – Influence of experimental procedures", *Mat. & Struc. (RILEM)*, **25**, 305–312.

HILLERBORG, A. MODÉER, M. and PETERSSON, P.-E. (1976). "Analysis of crack formation and crack growth in concrete by means of fracture mechanics and finite elements", *Cem. & Con. Res.*, **6**, 773–782.

HILLERBORG, A. (1985). "Influence of beam size on concrete fracture energy determination according to a draft R ILEM recommendation", *report TVBM-3021*, Lund Institute of Technology, Division of Building Materials, Lund, Sweden.

LINSBAUER, H.N. and TSCHEGG, E.K. (1986). "Fracture energy determination of concrete with cube shaped specimens", *Zement und Beton*, **31**, 38–40 (in German).

MANDELBROT, B.B. (1982). *The Fractal Geometry of Nature*, W.H. Freemann & Company, New York, USA.

ROTS, J.G. (1988). *Computational modelling of concrete fracture*, PhD-Thesis, Delft University of Technol ogy, Delft, The Netherlands.

STUIT, H.G. (1993). "The verification of numerical calculations with tests on sand in the geocentrifuge", *Topics in Applied Mechanics*, (eds. J.F. Dijksman & F.T.M. Nieuwstadt). Kluwer Academic Publishers, 73–80.

VAN MIER, J.G.M. (1991a). "Model fracture of concrete: discontinuous crack growth and crack interface grain bridging", *Cem. & Con. Res.*, **21**, 1–15.

VAN MIER, J.G.M. (1991b). "Crack face bridging in normal, high strength and Lytag concrete", *Fracture processes in concrete rock and ceramics*, (eds. J.G.M. Van Mier, J.G. Rots & A. Bakker). E.&F.N. Spon, London, 27–40.

VERVUURT, A (1996). PhD-Thesis, Delft University of Technology, Delft, The Netherlands (in preperation).

VERVUURT, A. and VAN MIER, J.G.M. (1994a). "Experimental and numerical analysis of boundary effects in uniaxial tensile tests", *Localized Damage III, Computer-aided assesment and control*, (eds. M.H. Aliabadi et al.). Computational Mechanics Publications, Southampton, 3–10.

VERVUURT, A. and VAN MIER, J.G.M. (1994b). "An optical technique for surface crack measurements of composite materials", *Recent Advances in Experimental Mechanics* (eds. S. Gomes et al.), Balkema, Rotterdam, 437–442.

VERVUURT, A. and VAN MIER, J.G.M. (1995). "Optical microscopy and digital image analysis of bondcracks in cement-based materials", *MRS Symposium Proc. vol. 370* (eds. S. Diamond et al.), Pittsburgh, USA.

ZHANG, M.H. and GJØRV, O.E. (1990). "Microstructure of the interfacial zone between lightweight aggregate and cement paste", *Cem. & Con. Res.*, **20**, 610–618.